

The Aquaporin Sidedness Revisited

Simon Scheuring¹, Peter Tittmann², Henning Stahlberg¹
Philippe Ringler¹, Mario Borgnia³, Peter Agre³, Heinz Gross²
and Andreas Engel^{1*}

¹M. E. Müller Institute for
Microscopy at the Biozentrum
University of Basel
Klingelbergstr. 70, CH-
4056, Basel, Switzerland

²Institute of Applied Physics
ETH Zürich, CH-8093, Zürich
Switzerland

³Department of Biological
Chemistry and Medicine, Johns
Hopkins University School of
Medicine, Baltimore, MD
21205-21850, USA

Aquaporins are transmembrane water channel proteins, which play important functions in the osmoregulation and water balance of microorganisms, plants, and animal tissues. All aquaporins studied to date are thought to be tetrameric assemblies of four subunits each containing its own aqueous pore. Moreover, the subunits contain an internal sequence repeat forming two obversely symmetric hemichannels predicted to resemble an hour-glass. This unique arrangement of two highly related protein domains oriented at 180° to each other poses a significant challenge in the determination of sidedness. Aquaporin Z (AqpZ) from *Escherichia coli* was reconstituted into highly ordered two-dimensional crystals. They were freeze-dried and metal-shadowed to establish the relationship between surface structure and underlying protein density by electron microscopy. The shadowing of some surfaces was prevented by protruding aggregates. Thus, images collected from freeze-dried crystals that exhibited both metal-coated and uncoated regions allowed surface relief reconstructions and projection maps to be obtained from the same crystal. Cross-correlation peak searches along lattices crossing metal-coated and uncoated regions allowed an unambiguous alignment of the surface reliefs to the underlying density maps. AqpZ topographs previously determined by AFM could then be aligned with projection maps of AqpZ, and finally with human erythrocyte aquaporin-1 (AQP1). Thereby features of the AqpZ topography could be interpreted by direct comparison to the 6 Å three-dimensional structure of AQP1. We conclude that the sidedness we originally proposed for aquaporin density maps was inverted.

© 2000 Academic Press

Keywords: aquaporin Z; aquaporin 1; atomic force microscopy; water channel; metal-shadowing

*Corresponding author

Introduction

To maintain metabolic processes water molecules must efficiently permeate the plasma membranes of cells in all living organisms. Since the diffusion of water molecules through lipid bilayers has an activation energy >10 kcal/mol (Chandy *et al.*, 1997), the existence of specific water pores was postulated more than four decades ago (Sidel & Solomon, 1957). The first member of this family termed the aquaporins (Chrispeels & Agre, 1994) and designed by evolution to facilitate water trans-

port, was identified by Preston *et al.* (1992). Aquaporin sequences share six hydrophobic stretches, which correspond to transmembrane helices. Two long conserved loops, B and E, connect helices 2 and 3, and 5 and 6, respectively, and accommodate the highly conserved NPA motifs (Gorin *et al.*, 1984; Preston & Agre, 1991). These loops fold back into the membrane, to form the structure of the pore (Jung *et al.*, 1994). Permeability studies by stopped flow measurements indicate flow rates in the range of 10⁹ water molecules per channel and per second, and an activation energy <5 kcal/mol (Walz *et al.*, 1994b; Zeidel *et al.*, 1992).

Aquaporin-1 (AQP1) of human erythrocytes (Agre *et al.*, 1993) is structurally the best studied aquaporin. Two-dimensional (2D) crystals with two tetramers packed in opposite orientation into a unit cell with dimensions of $a = b = 96 \text{ \AA}$ and

Abbreviations used: AQP1, aquaporin-1; AqpZ, aquaporin Z; AFM, atomic force microscopy.

E-mail address of the corresponding author:
andreas.engel@unibas.ch

$\gamma = 90^\circ$ have been reconstituted in the presence of lipids (Walz *et al.*, 1994a). These highly ordered 2D crystals diffracted a 300 kV electron beam to at least 3.5 Å resolution (Mitsuoka *et al.*, 1999). A 3D density map at 6 Å resolution calculated from projections of samples tilted with respect to the electron beam, revealed a right-handed bundle consisting of six transmembrane α -helices surrounding a central density (Walz *et al.*, 1997; Cheng *et al.*, 1997), in agreement with sequence-based structure prediction. The central density formed by the long loops B and E has recently been resolved as two short helices projecting outwards from the center of the monomer which are connected to adjacent helices by loop regions (Mitsuoka *et al.*, 1999), thus confirming the hour-glass model (Jung *et al.*, 1994).

The *Escherichia coli* water channel AqpZ has been identified by expression cloning (Calamita *et al.*, 1995) and overexpressed in its native system (Borgnia *et al.*, 1999). This bacterial water channel maintains cell turgor during the volume expansion of cell division (Calamita *et al.*, 1998). Highly ordered 2D crystals have been grown by dialysis of protein-lipid-detergent mixtures (Ringler *et al.*, 1999). The square unit cells with dimensions $a = b = 95$ Å, $\gamma = 90^\circ$, contained eight monomers and had $p4_2$ symmetry (Ringler *et al.*, 1999). Cryo-electron microscopy provided a projection map at 7 Å resolution exhibiting the characteristic features of AQP1 consistent with the high sequence homology of the aquaporins (Ringler *et al.*, 1999). These 2D crystals were assembled from AqpZ bearing an N-terminal fragment of 26 amino acids containing ten histidine residues. AFM studies before and after removal of this N-terminal fragment with trypsin, allowed the sidedness of AqpZ surfaces to be unambiguously assigned (Scheuring *et al.*, 1999). The crown-like extracellular side possesses three protrusions of 7 Å height per monomer, of which the largest one was identified as loop C, which comprises 26 amino acid residues. One protrusion per monomer was visible on the cytoplasmic surface, probably resulting from loops B and/or D (Scheuring *et al.*, 1999).

In contrast, the sidedness of AQP1 has been determined using surface relief reconstruction of metal-shadowed AQP1 2D crystals before and after digestion with carboxypeptidase Y (Walz *et al.*, 1996). Although these results promoted a straightforward interpretation, the recent 4.5 Å 3D density map by Mitsuoka *et al.* (1999) suggested a different assignment of the sidedness. Therefore, we analyzed freeze-dried AqpZ 2D crystals that were partially metal-shadowed to calculate both surface reliefs and projection maps of one and the same crystal. In this way the sidedness of the AqpZ projection map could be identified and related to that of AQP1. The results presented here suggest that the sidedness of AQP1 previously reported by Walz *et al.* (1996) has to be revised.

Results

Trypsin-digested AqpZ 2D crystals adsorbed to glow-discharged carbon films were washed in distilled water, and quickly frozen in liquid nitrogen. After freeze-drying and deposition of a 5 Å thick heavy-metal film (see Walz *et al.*, 1996), the crystals were imaged at a temperature of -180°C at doses below 5 electrons/Å². Overview images (Figure 1(a)) were taken with the Gatan slow scan CCD camera at a magnification of 4000 \times and directly used to position crystalline areas for low-dose imaging at high magnification. To this end, tightly adsorbed, flat single-layered sheets were selected (see Figure 1(a)).

Overview images of metal-shadowed samples (Figure 1(a); arrow top right indicates the shadowing direction) were carefully searched for the borderlines of metal-coating (indicated by the black and the white arrows in Figure 1(a)). Unshadowed areas resulted when aggregates (indicated by the asterisk in Figure 1(a)) blocked the metal beam. Areas such as that outlined by the square in Figure 1(a) were then recorded at a magnification of 45,000 \times (5 Å/pixel on the CCD camera, Figure 1(b)), yielding a large number of unit cells from the freeze-dried, metal-shadowed area and from the uncoated area. Raw data of shadowed areas appear dark (Figure 1(b), top left), while uncoated areas are bright (Figure 1(b), bottom right). Such images were Fourier peak filtered to produce a first reference for a cross-correlation peak search on both the metal-coated and the uncoated areas (Figure 1(b), the cross-correlation peaks on the metal-shadowed area are indicated by squares, on the uncoated area by crosses). A lattice yielding the perpendicular vectors of 95 Å length was fitted to the correlation peaks with a tolerance of 0.05 (4.75 Å). Figure 1(c) displays the cross-correlation average of the 971 unit cells (white frame indicates the unit cell) found on the metal-coated area in Figure 1(b). Adjacent tetramers have a different appearance due to the up and down packing of the particles within the crystal. As a consequence of unidirectional shadowing (arrow top right indicates the shadowing direction) the 4-fold symmetry is lost. Figure 1(d) (white frame indicates the unit cell) shows the 4-fold symmetrized surface relief reconstruction of Figure 1(c) (see Fuchs *et al.*, 1995; Kistler *et al.*, 1977; Guckenberger, 1985). The pixel sampling of 5 Å prevented resolution of fine substructures in this average, but the orientation of the lipid-filled rhombus between adjacent tetramers, and the height difference of the tetramers with respect to each other is distinct. The projection average of 1444 unit cells of the uncoated freeze-dried area (Figure 1(e), white frame indicates the unit cell) reveals the tetramer organization and orientation within the crystal lattice. Probably as a result of interactions between the crystal and the carbon film or residual metal shadowing, neighboring particles differ slightly in brightness. Nevertheless, the

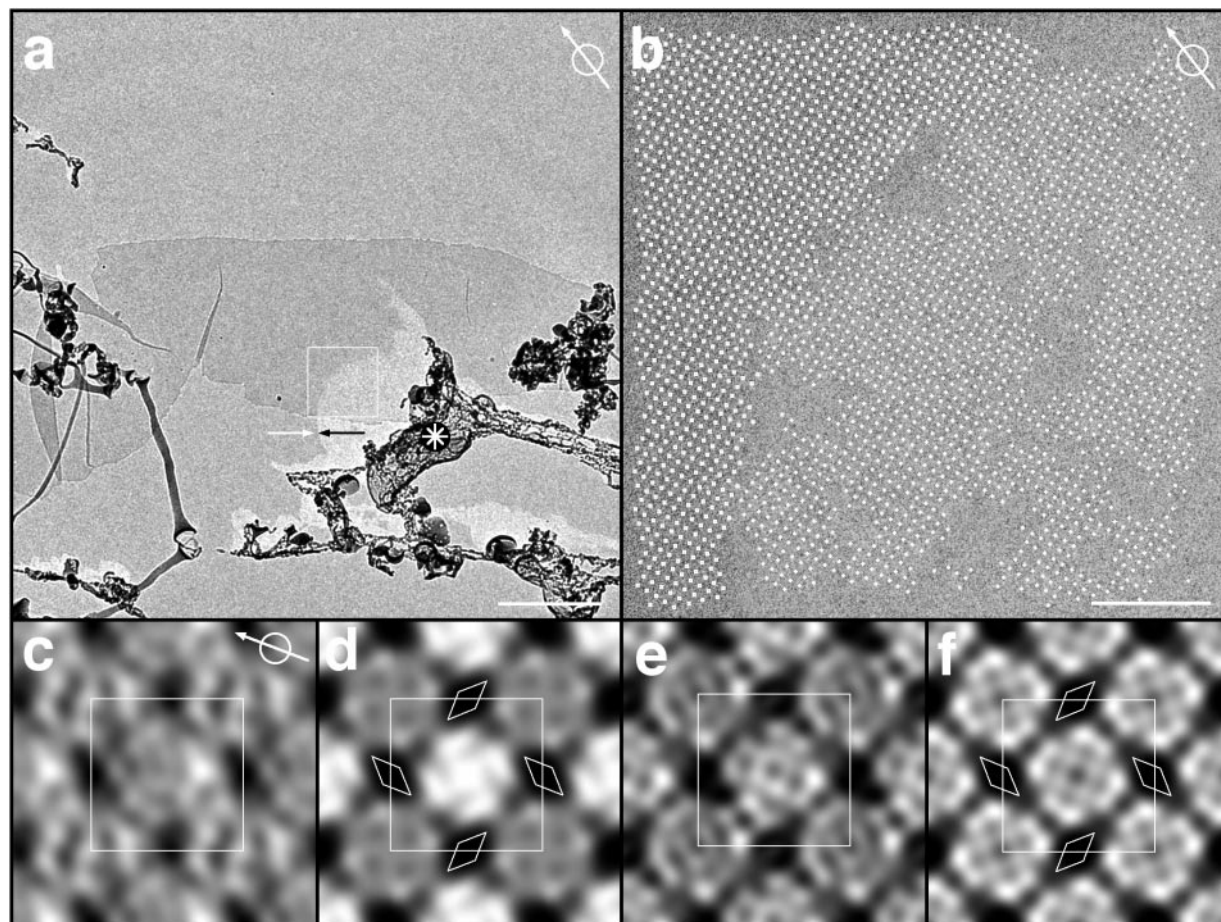


Figure 1. (a) Overview image of a freeze-dried and subsequently metal-shadowed crystalline sheet of AqpZ adsorbed to a carbon-coated electron microscopy grid. The black and white arrows pointing towards each other indicate the borderline of metal-coated and uncoated areas. The asterisk indicates the aggregate, which prevented parts of the crystal from metal deposition (compare aggregate and shadow borderline). The white frame defines the position of the following higher magnification image. The shadowing azimuth is indicated in the top right (the scale bar represents 1 μm). (b) Low-dose image of the area outlined in (a). The metal-shadowed side (top left) is darker than the uncoated region (bottom right). The squares ($n = 971$) and crosses ($n = 1444$) indicate unit cell positions on the metal-coated side and on the uncoated side, respectively, which fitted with a displacement tolerance smaller than 0.05 (4.75 \AA) to the square lattice of 95 \AA . The shadowing azimuth is given in the top right (the scale bar represents 100 nm). (c) Correlation average of the 971 unit cells found on the unidirectionally metal-shadowed area. The 4-fold symmetry of the tetramers is lost due to the unidirectional metal deposition. The shadowing azimuth is displayed in the top right (the white frame indicates the unit cell: 95 $\text{\AA} \times 95 \text{\AA}$). (d) The 4-fold symmetrized surface reconstruction of the cross-correlation average displayed in (c) (the white frame indicates the unit cell: 95 $\text{\AA} \times 95 \text{\AA}$). Rhombi surrounding the higher, extracellular surface form a right-handed windmill-like structure. (e) Correlation average of the 1444 unit cells found on the uncoated freeze-dried area. The 4-fold symmetry of the tetramers is preserved. Adjacent tetramers appear with different brightness probably due to crystal - carbon film interaction (white frame indicates unit cell: 95 $\text{\AA} \times 95 \text{\AA}$). (f) $p42,2$ symmetrized projection map of the cross-correlation average displayed in (e) (the white frame indicates the unit cell: 95 $\text{\AA} \times 95 \text{\AA}$). The central tetramer is the view from the extracellular side (corresponding to the central particle in (d)) and is surrounded by rhombi forming a right-handed windmill-like structure.

appearance of adjacent tetramers is very similar and the 4-fold symmetry is essentially preserved. After $p42,2$ symmetrization (Figure 1(f), white frame indicates the unit cell) the rotation of the particles with respect to each other and the orientation of the rhombus-shaped lipid interspace is clearly visible. From Figure 1 we conclude that the surface protruding most from the lipid bilayer (central tetramer in Figure 1(d)) corresponds to the tetramer similarly surrounded by rhombi in right-handed orientation in the projection map (central tetramer in Figure 1(f)). As previously reported,

the most protruding surface is extracellular (Scheuring *et al.*, 1999). Therefore, this central tetramer represents the projection from the extracellular side.

To obtain higher-resolution structural information, images of both metal-coated and uncoated crystals were recorded at a magnification of $77,000\times$ (3.1 $\text{\AA}/\text{pixel}$ on the CCD camera). The unit cell dimensions were found to be $a = b = 95(\pm 1) \text{\AA}$ and $\gamma = 90(\pm 1)^\circ$ ($n = 25$). Surface relief reconstructions from such images of unidirectionally metal-shadowed AqpZ crystals had a

resolution of 12 Å (Figure 2(b)). The average surface relief obtained from the metal-shadowed specimen (Figure 2(b)) is consistent with the average resulting from high-resolution AFM topographs (Figure 2(a); Scheuring *et al.*, 1999) in that both exhibit one strongly and one weakly protruding tetramer. The two averages also correlate favorably in the topology along the periphery of the higher extracellular surface, the strong indentation in the center of the cytoplasmic surface, and the overall particle organization. However the inner ring of protruding structures on the extracellular surface is oriented differently in the AFM topograph and the outer ring protrusions of the cytoplasmic surface of the reconstructed relief are more pronounced than the features determined with the AFM.

A projection map was calculated to 12 Å resolution from the unshadowed freeze-dried crystal areas (Figure 2(c)). This map is very similar to the cryo electron microscopy projection map with a resolution of 7 Å (Figure 2(d); Ringler *et al.*, 1999). The tetramers show an inner ring of densities close to their 4-fold symmetry center and an outer ring of densities along their periphery. The monomers can be distinguished and the opposite rotation of adjacent tetramers with respect to the lattice lines leading to rhombus-shaped lipid interspaces is evident. These features allow the unambiguous alignment of the two maps (Figure 2(c) and (d)).

The extracellular and cytoplasmic topologies revealed by AFM experiments (Scheuring *et al.*, 1999) are shown in Figure 3(a) and (b), respectively. Corresponding regions of the projection map of AqpZ are shown aligned in Figure 3(c) and (d), respectively. Finally, Figure 3(e) and (f) show the projection map of AQP1 aligned with respect to

that of AqpZ (Figure 3(c) and (d)). This alignment is compatible with that reported by Ringler *et al.* (1999), but it has been improved by considering the 1% difference of the unit cell size. This improvement yielded a correlation coefficient of 78% after a clockwise rotation of the AQP1 tetramer (Figure 3(e)) by 15°. If, however the AQP1 tetramer shown in Figure 3(f) is rotationally aligned with AqpZ in Figure 3(c), the correlation coefficient is 65%, allowing the unambiguous assignment of the AQP1 projection map in Figure 3(e) as extracellular. To relate protrusions observed by AFM with loops or protruding helices, the projection maps are overlaid by the topography contours.

Figure 4(a) and (b) display perspective views of the 3D map of AQP1 at 6 Å resolution from the extracellular and the cytoplasmic side, respectively. α -Helices are represented as gray sausages, the bright parts of which display the ends facing the viewer. The map is overlaid by contours of protrusions imaged by AFM under native conditions (see Figure 3(a) and (b)). Flexible parts of proteins, such as loops, are mostly averaged out, hence the AFM topography implements additional information on the organization of the non-membrane-stabilized protein structure to the 3D density map.

Discussion

AFM investigations of densely packed or regularly arranged membrane protein layers can provide information on their sidedness in conjunction with either proteolytic cleavage of a terminal domain (Scheuring *et al.*, 1999), or specific binding of antibodies (Müller *et al.*, 1996). The sidedness of AqpZ surfaces has been unambiguously defined by imaging crystals before and after proteolytic

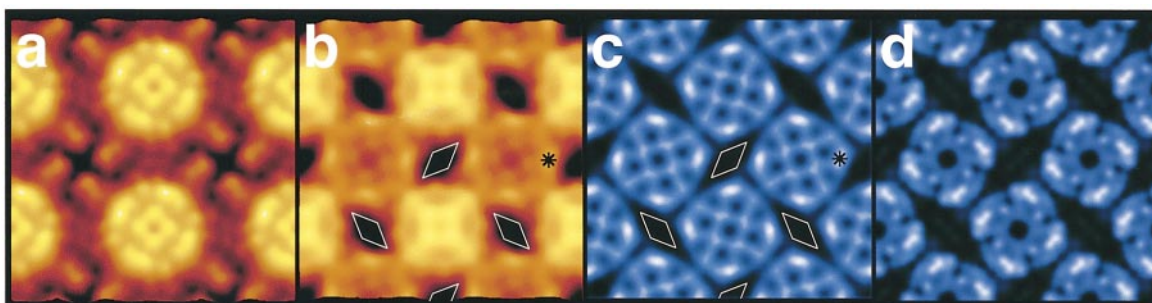


Figure 2. Correlation between surface topography and electron density projection map (panel sidelengths 190 Å). (a) Average of high-resolution AFM topographies (10° tilted surface representation) of trypsin-digested AqpZ 2D crystals imaged in buffer solution. The crown-like extracellular surface protrudes 7 Å out of the lipid bilayer, while the cytoplasmic surface only protrudes by 3.5 Å (Scheuring *et al.*, 1999). (b) Surface reconstruction (10° tilted surface representation) of freeze-dried unidirectionally metal-shadowed AqpZ 2D crystals. As indicated, right-hand oriented rhombus-shaped lipid interspaces surround the extracellular surface. The asterisk indicates the position of protruding structure in the metal-shadowing surface reconstruction map, which is not present in the topography recorded by the AFM. (c) Average density map of freeze-dried AqpZ 2D crystals. As indicated, right-hand oriented rhombus-shaped lipid interspaces surround the projection viewed from the extracellular side. The asterisk marks protein density which induces a protrusion signal in the surface reconstruction (indicated by asterisk in (b)). (d) Average density map of cryo-electron micrographs from trehalose-embedded AqpZ 2D crystals (Ringler *et al.*, 1999).

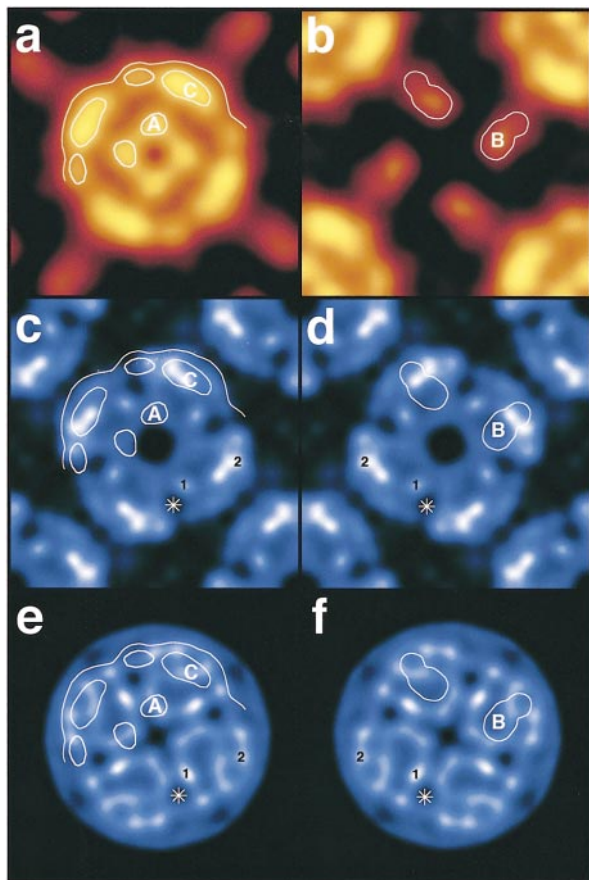


Figure 3. Overlay of AqpZ AFM topography recorded in buffer solution on projection maps of AqpZ and AQP1, both rendered at 7 Å resolution (full frame sizes 95 Å). (a) AFM topography of the extracellular surface of AqpZ with outlined and annotated protrusions and overall shape (see Discussion; Scheuring *et al.*, 1999). (b) AFM topograph of the cytoplasmic surface of AqpZ with outlined protrusions housing non-membrane buried parts of loop B (see Discussion; Scheuring *et al.*, 1999). (c) Projection map of AqpZ (Ringler *et al.*, 1999) viewed from the extracellular side. Outlines of corresponding surface protrusions are overlaid: loop C is at the periphery and spans a major part of a monomer. (d) Projection map of AqpZ (Ringler *et al.*, 1999) viewed from the cytoplasmic side. Outlines of corresponding surface protrusions are overlaid: non-membrane-buried parts of loop B (comprising the NPA motif which participates in the water pore) cross the center of one monomer. (e) Projection map of AQP1 (Walz *et al.*, 1995) viewed from the extracellular side after an applied clockwise rotation of 15°. Protrusions are outlined as in (c). (f) Projection map of AQP1 (Walz *et al.*, 1995) viewed from the cytoplasmic side after an applied counterclockwise rotation of 15°. Protrusions are outlined as in (d). The maximum rotational alignment cross-correlation coefficient was obtained when the lowest density between monomers (indicated by the asterisk) and of asymmetric densities within the monomer (indicated by 1 and 2) were superimposed.

cleavage of the cytoplasmic N terminus identifying the 7 Å high crown-like surface as extracellular (Figure 2(a); Scheuring *et al.*, 1999).

To link topographical data obtained by AFM with the projection structure acquired by electron crystallography, we have analyzed freeze-dried crystals that were partially metal-shadowed. As illustrated in Figure 1, surface reliefs calculated from metal-coated areas were thus in register with projection maps from uncoated areas of the same crystal, allowing the unambiguous assignment of topography and projection map. This novel approach is of particular advantage for aquaporins whose quasi 2-fold symmetry makes the assignment of the sidedness difficult (Mitsuoka *et al.*, 1999).

The experiment described here can be applied in general, provided that large, coherent 2D crystals are available. It has been designed to solve the discrepancy between the sidedness assignment of AQP1 by Walz *et al.* (1996) and the 4.5 Å 3D density map by Mitsuoka *et al.* (1999). The regions assigned to loop B and E in the latter map suggest a sidedness opposite to that proposed by Walz *et al.* (1996). Since AFM experiments allowed the sidedness of AqpZ topographies to be assigned firmly (Scheuring *et al.*, 1999), and because AqpZ projection maps could be aligned with those of AQP1 (Figure 3; Ringler *et al.*, 1999), establishing the link between relief reconstruction and projection map appeared to be a straight-forward approach to settle this pertinent question. The experimental results documented in Figures 1 and 2 provide a solid basis to align the surface topography of AqpZ recorded by AFM to 7 Å resolution with the projection map of AQP1 (Figure 3) and hence with the 3D map of AQP1 (Figure 4).

A recent sequence alignment study of 160 aquaporin sequences revealed highly conserved residues within all helical segments (Heymann & Engel, 2000). Together with the general similarity of projection maps from different aquaporins (Fotiadis *et al.*, 2000; Daniels *et al.*, 1999) this suggests a conserved helical packing arrangement. From helical periodicity analysis Heymann & Engel (2000) proposed a helix assignment that is indicated in Figure 4. This assignment is consistent with the findings from fitting helical stretches to elongated structures in the 4.5 Å 3D density map (B.L. de Groot *et al.*, personal communication). Therefore, the contoured protrusions of AqpZ overlaid on the 3D map of AQP1 are highly relevant. They provide a solid basis to select the most likely helix assignment from the two possibilities given by Heymann & Engel (2000). Figure 4(a) indicates that the peripheral protrusion C is likely to connect helices 3 and 4. This is compatible with the assignment of this protrusion to loop C based on volume calculations and flexibility mapping by AFM (Scheuring *et al.*, 1999). The previously unassigned peripheral protrusion on the extracellular surface appears to be the C-terminal end of helix 3. Thus, the other protrusion, now labeled A, must represent loop A, in agreement with the helical assignment by Heymann & Engel (2000). Since loop D is short in all aquaporins and the N and C

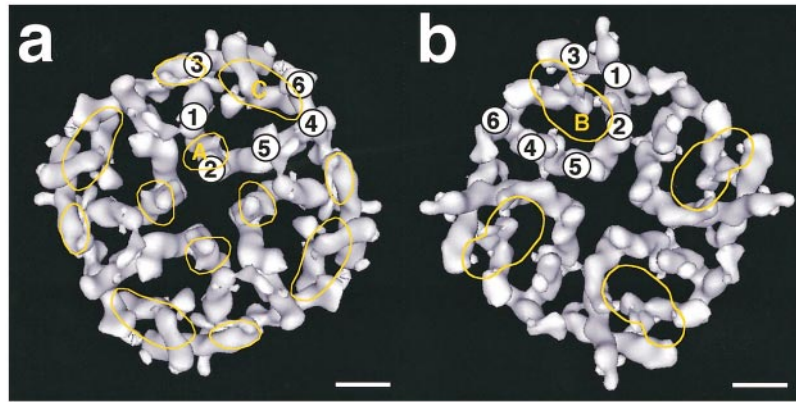


Figure 4. Surface-rendered 3D electron density map of AQP1 at 6 Å resolution (Walz *et al.*, 1997). The right-handed bundle of the six transmembrane-spanning α -helices is aligned according to the projection maps in Figure 3(e) and (f). Superposed contours indicate the topographical features of AqpZ 2D crystals measured by AFM in buffer solution. Helix assignment is as proposed by Heymann & Engel (2000). (a) View from the extracellular side, with assigned loops indicated. The small protrusion on the periphery might be part of loop

C, which connects the end of helix 3 with the beginning of helix 4 (see Discussion). (b) View from the cytoplasmic side. The AFM topograph shows one protrusion corresponding to parts of loop B which spans the water pore (see Discussion).

termini are almost completely removed by trypsin digestion of AqpZ 2D crystals (Scheuring *et al.*, 1999), the protrusion contoured in Figure 4(b) is likely to present the surface of loop B that folds back into the membrane and connects helices 2 and 3. The position and shape of this protrusion further confirm the helical assignment shown in Figure 4.

Taken together, compelling evidence has been accumulated to justify revision of the sidedness assignment proposed by Walz *et al.* (1996). The pertinent question arises as to how apparently solid data could have been misinterpreted. A possible explanation is related to the observation that carboxypeptidase Y treatment in solution tends to produce disordered crystals and aggregates (B. Heymann, D. Fotiadis & D. J. Müller, unpublished results). Therefore, the few crystals found by Walz *et al.* (1996) after decarboxylation may not have been properly digested. The structural differences however, may have resulted from lattice disorder and surface contamination by proteolytic fragments.

The alignment of the AqpZ topography with the AQP1 3D map corroborates the topology of AQP1 derived from fitting helical stretches using the program ROTTRANS (B.L. de Groot *et al.*, personal communication) to the 4.5 Å 3D density map (Mitsuoka *et al.*, 1999) and the helix assignment from sequence analysis (Heymann & Engel, 2000). With the sidedness issue resolved, the overall architecture of AQP1 is now established and will help in tracing the polypeptide in higher-resolution electron crystallographic analysis.

Materials and Methods

2D crystallization

2D crystals were produced by dialysis of solubilized AqpZ (1 mg/ml, in 2% octyl- β -D-glucopyranoside (OG)) mixed with 1-palmitoyl-2-oleoyl-*sn*-glycero-3-phosphocholine (POPC)/1,2-dimiristoyl-*sn*-glycero-3-phosphocholine (DMPC) 1:1 (from Avanti Polar Lipids, Inc.,

USA) in 2% OG (from Anatrace, Inc., USA) at a lipid to protein ratio of 0.4 against a detergent-free buffer (10 mM citrate (pH 6), 200 mM NaCl, 100 mM MgCl₂, 10% (v/v) glycerol, 0.005% (w/v) NaN₃) (Ringler *et al.*, 1999). Crystals were harvested after three days.

Trypsin digestion

For cleavage of the N-terminal fragment, AqpZ-10his crystals were incubated overnight at 4°C with trypsin (1 mg/ml). After trypsin treatment samples were investigated by sodium dodecyl sulfate-polyacrylamide gel electrophoresis SDS-PAGE using 10% (w/v) acrylamide gels (data not shown, for details see Scheuring *et al.*, 1999).

Atomic force microscopy

AqpZ 2D crystals were deposited onto freshly cleaved muscovite mica (from Mica New York Corp., New York, USA) and imaged in buffer solution (10 mM Tris-HCl (pH 7.2), 150 mM NaCl) at high resolution (for details see Scheuring *et al.*, 1999).

Freeze-drying and metal-shadowing

AqpZ crystals were adsorbed (two minutes) to glow-discharged (one minute) carbon-coated 400-mesh grids. These were washed twice with double-distilled water, blotted and plunged into liquid nitrogen. The grids were then freeze-dried and metal-shadowed in the MIDILAB (Gross *et al.*, 1990), as detailed by Walz *et al.* (1996). After shadowing, grids were transferred to a specially designed Gatan cryo holder, and examined. Images were digitally recorded with a Gatan-694 slow scan CCD camera with a maximal image size of 1024² pixels. Images were correlation averaged using the SEMPER image processing package (Saxton *et al.*, 1979), while surface reconstructions of metal-shadowed crystals were calculated in SEMPER or MILAN (Fuchs *et al.*, 1995) image processing packages. The handedness determined by the sample orientation in the microscope, the image acquisition with the CCD camera, and the data transfer to various processing systems were carefully controlled by coadsorption of amyloid fibrils.

Cryo electron microscopy

AqpZ 2D crystals mixed with 3-10% trehalose were adsorbed to carbon-coated copper electron microscopy grids. The grids were blotted and plunged into liquid ethane. Vitrified specimens were recorded in a Hitachi H8000 electron microscope with a LaB₆ filament, operated at 200 kV under low-dose conditions (~5 e⁻/Å²) and processed using the MRC image processing package (for details see Ringler *et al.*, 1999).

Acknowledgments

We thank Dr Claire Goldsbury, who provided the amyloid fibers coadsorbed with the AqpZ crystals to overcome handedness problems. We acknowledge fruitful discussions with Dr S. A. Müller, who helped in assembling the manuscript. This work was supported by the Swiss National Foundation for Scientific Research (grant 4036-44062 to A. E.), the Swiss Priority Project for Micro and Nano System Technology (MINAST), the Maurice E. Müller Foundation of Switzerland and the National Institutes of Health (to P. A.).

References

- Agre, P., Preston, G., Smith, B., Jung, J., Raina, S., Moon, C., Guggino, W. & Nielsen, S. (1993). Aquaporin CHIP: the archetypal molecular water channel. *Am. J. Physiol.* **265**, F436-F476.
- Borgnia, M., Kozono, D., Calamita, G., Maloney, P. C. & Agre, P. (1999). Functional reconstitution and characterization of AqpZ, the *E. coli* water channel protein. *J. Mol. Biol.* **29**, 1169-1179.
- Calamita, G., Bishai, W., Preston, G., Guggino, W. & Agre, P. (1995). Molecular cloning and characterization of AQPZ, a water channel from *Escherichia coli*. *J. Biol. Chem.* **270**, 29063-29066.
- Calamita, G., Kempf, B., Bonhivers, M., Bishai, W. R., Bremer, E. & Agre, P. (1998). Regulation of the *Escherichia coli* water channel gene AqpZ. *Proc. Natl Acad. Sci. USA*, **95**, 3627-3631.
- Chandy, G., Zampighi, G. A., Kreman, M. & Hall, J. E. (1997). Comparison of the water transporting properties of MIP and AQP1. *J. Membr. Biol.* **159**, 29-39.
- Cheng, A., van Hoek, A. N., Yeager, M., Verkman, A. S. & Mitra, A. K. (1997). Three-dimensional organization of a human water channel. *Nature*, **387**, 627-630.
- Chrispeels, M. & Agre, P. (1994). Aquaporins: water channel proteins of plant and animal cells. *Trends Biochem. Sci.* **19**, 421-425.
- Daniels, M. J., Chrispeels, M. J. & Yeager, M. (1999). Projection structure of a plant vacuole membrane aquaporin by electron cryo-crystallography. *J. Mol. Biol.* **294**, 1337-1349.
- Fotiadis, D., Hasler, L., Müller, D. J., Stahlberg, H., Kistler, J. & Engel, A. (2000). The surface topography of lens MIP supports dual functions. *J. Mol. Biol.* In the press.
- Fuchs, K., Tittmann, P., Krusche, K. & Gross, H. (1995). Reconstruction and representation of surface data from two-dimensional crystalline, biological macromolecules. *Bioimaging*, **3**, 12-24.
- Gorin, M. B., Yancey, S. B., Cline, J., Revel, J.-P. & Horwitz, J. (1984). The major intrinsic protein (MIP) of the bovine lens fiber membrane: characterization and structure based on cDNA cloning. *Cell*, **39**, 49-59.
- Guckenberger, R. (1985). Surface relief derived from heavy-metal-shadowed specimen-Fourier space techniques applied to periodic objects. *Ultramicroscopy*, **16**, 357-370.
- Heymann, J. B. & Engel, A. (2000). Structural clues in the sequences of the aquaporins. *J. Mol. Biol.* **295**, 1039-1053.
- Heymann, J. B., Müller, D. J., Landau, E. M., Rosenbusch, J. P., Pebay-Peyroula, E., Büldt, G. & Engel, A. (1999). Charting the surfaces of purple membrane. *J. Struct. Biol.* **128**, 243-249.
- Jung, J., Preston, G., Smith, B., Guggino, W. & Agre, P. (1994). Molecular structure of the water channel through aquaporin CHIP. The hourglass model. *J. Biol. Chem.* **269**, 14648-14654.
- Kistler, J., Aebi, U. & Kellenberger, E. (1977). Freeze-drying and shadowing a two-dimensional periodic specimen. *J. Ultrastruct. Res.* **59**, 76-86.
- Li, H., Lee, S. & Jap, B. K. (1997). Molecular design of aquaporin-1 water channel as revealed by electron crystallography. *Nature Struct. Biol.* **4**, 263-265.
- Mitsuoka, K., Murata, K., Walz, T., Hirai, T., Agre, P., Heymann, J. B., Engel, A. & Fujiyoshi, Y. (1999). The structure of aquaporin-1 at 4.5-Å resolution reveals short α -helices in the center of the monomer. *J. Struct. Biol.* **128**, 34-43.
- Mulders, S., Preston, G., Deen, P., Guggino, W., Van, O. C. & Agre, P. (1995). Water channel properties of major intrinsic protein of lens. *J. Biol. Chem.* **270**, 9010-9016.
- Müller, D. J. & Engel, A. (1999). pH and voltage induced structural changes of porin OmpF explain channel closure. *J. Mol. Biol.* **285**, 1347-1451.
- Müller, D. J., Schoenenberger, C. A., Büldt, G. & Engel, A. (1996). Immuno-atomic force microscopy of purple membrane. *Biophys. J.* **70**, 1796-1802.
- Preston, G. M. & Agre, P. (1991). Isolation of the cDNA for erythrocyte integral membrane protein of 28 kilodaltons: member of an ancient channel family. *Proc. Natl Acad. Sci. USA*, **88**, 11110-11114.
- Preston, G. M., Carroll, T. P., Guggino, W. B. & Agre, P. (1992). Appearance of water channels in *Xenopus* oocytes expressing red cell CHIP28 protein. *Science*, **256**, 385-387.
- Ringler, P., Borgnia, M., Stahlberg, H., Agre, P. & Engel, A. (1999). Structure of the water channel AqpZ from *Escherichia coli* revealed by electron crystallography. *J. Mol. Biol.* **291**, 1181-1190.
- Saxton, W. O., Pitt, J. T. & Horner, M. (1979). The SEMPER image processing system. *Ultramicroscopy*, **4**, 343-354.
- Schabert, F. A., Henn, C. & Engel, A. (1995). Native *Escherichia coli* OmpF porin surfaces probed by atomic force microscopy. *Science*, **268**, 92-94.
- Scheuring, S., Ringler, P., Borgnia, M., Stahlberg, H., Agre, P. & Engel, A. (1999). High resolution AFM topographs of the *Escherichia coli* waterchannel aquaporin Z. *EMBO J.* **18**, 4981-4987.
- Sidel, V. W. & Solomon, A. K. (1957). Entrance of water into human red cells under an osmotic pressure gradient. *J. Gen. Physiol.* **41**, 243-257.
- Walz, T., Smith, B., Agre, P. & Engel, A. (1994a). The three-dimensional structure of human erythrocyte aquaporin CHIP. *EMBO J.* **13**, 2985-2993.

- Walz, T., Smith, B., Zeidel, M., Engel, A. & Agre, P. (1994b). Biologically active two-dimensional crystals of aquaporin CHIP. *J. Biol. Chem.* **269**, 1583-1586.
- Walz, T., Typke, D., Smith, B. L., Agre, P. & Engel, A. (1995). Projection map of aquaporin-1 determined by electron crystallography. *Nature Struct. Biol.* **2**, 730-732.
- Walz, T., Tittmann, P., Fuchs, K. H., Müller, D. J., Smith, B. L., Agre, P., Gross, H. & Engel, A. (1996). Surface topographies at subnanometer resolution reveal asymmetry and sidedness of aquaporin-1. *J. Mol. Biol.* **264**, 907-918.
- Walz, T., Hirai, T., Murata, K., Heymann, J. B., Mitsuoka, A., Fujiyoshi, Y., Smith, B. L., Agre, P. & Engel, A. (1997). The 6 Å three-dimensional structure of aquaporin-1. *Nature*, **387**, 624-627.
- Zeidel, M. L., Ambudkar, S. V., Smith, B. L. & Agre, P. (1992). Reconstitution of functional water channels in liposomes containing purified red cell CHIP28 protein. *Biochemistry*, **31**, 7436-7440.

Edited by W. Baumeister

(Received 16 February 2000; received in revised form 12 April 2000; accepted 12 April 2000)